Engineering tunnel junctions on ballistic semiconductor nanowires

Cite as: Appl. Phys. Lett. 115, 043503 (2019); https://doi.org/10.1063/1.5108539 Submitted: 30 April 2019 . Accepted: 09 July 2019 . Published Online: 25 July 2019

J. Damasco, S. T. Gill, S. Gazibegovic 🗓, G. Badawy, E. P. A. M. Bakkers, and N. Mason







ARTICLES YOU MAY BE INTERESTED IN

In-phase supermode operation in GaN-based vertical-cavity surface-emitting laser Applied Physics Letters 115, 041101 (2019); https://doi.org/10.1063/1.5104289

Design of compositionally graded contact layers for MOCVD grown high Al-content AlGaN transistors

Applied Physics Letters 115, 043502 (2019); https://doi.org/10.1063/1.5108529

Low-temperature behaviors of multilayer MoS₂ transistors with ohmic and Schottky contacts Applied Physics Letters 115, 033501 (2019); https://doi.org/10.1063/1.5099380





Engineering tunnel junctions on ballistic semiconductor nanowires

Cite as: Appl. Phys. Lett. **115**, 043503 (2019); doi: 10.1063/1.5108539 Submitted: 30 April 2019 · Accepted: 9 July 2019 · Published Online: 25 July 2019







J. Damasco, S. T. Gill, S. Gazibegovic, G. Badawy, E. P. A. M. Bakkers, and N. Mason, D. Damasco, S. T. Gill, S. Gazibegovic, G. Badawy, G. Badawy, E. P. A. M. Bakkers, G. Badawy, G. Badawy, G. Badawy, G. Bakkers, G. Badawy, G. Bad

AFFILIATIONS

- ¹Department of Physics, University of Illinois at Urbana-Champaign, Urbana, Illinois 61801, USA
- ²Department of Applied Physics, Eindhoven University of Technology, 5600 MB Eindhoven, The Netherlands
- ³QuTech and Kavli Institute of NanoScience, Delft University of Technology, 2600 GA Delft, The Netherlands

ABSTRACT

Typical measurements of nanowire devices rely on end-to-end measurements to reveal mesoscopic phenomena such as quantized conductance or Coulomb blockades. However, creating nanoscale tunnel junctions allows one to directly measure other properties such as the density of states or electronic energy distribution functions. In this paper, we demonstrate how to realize uniform tunnel junctions on InSb nanowires, where the low invasiveness preserves ballistic transport in the nanowires. The utility of the tunnel junctions is demonstrated via measurements using a superconducting tunneling probe, which reveal nonequilibrium properties in the open quantum dot regime of an InSb nanowire. The method for high-quality tunnel junction fabrication on InSb nanowires is applicable to other III–V nanowires and enables characterization of nanowire local density of states.

Published under license by AIP Publishing. https://doi.org/10.1063/1.5108539

InSb nanowires provide a versatile platform for electrical devices as a result of high mobility, large spin-orbit coupling, and the ability to be extended to nanowire networks.3 Previous measurements of InSb nanowire devices have focused on end-to-end transport measurements, which have demonstrated coherent mesoscopic phenomena such as quantized conductance, quantum interference, and Josephson effect. However, improved understanding of these materials can be gained by utilizing tunneling spectroscopy, which can directly probe the electronic density of states (DOS). For example, a long-standing goal in the study of ballistic, semiconducting nanowires with strong spin-orbit coupling is to demonstrate helical modes, which can provide the basis for spintronic applications⁶ and engineering topological superconductivity. While it has been a challenge to detect helical modes using endto-end transport measurements as a result of sensitivity to chemical potential variations,8 it may be possible to detect these modes using momentum-resolved tunneling spectroscopy.69

Despite the interest in using InSb nanowires in electrical devices, the basic features such as the DOS and energy dispersion are not known a priori and determining these features for individual wires is challenging. For example, InSb nanowires are not well-suited for techniques such as scanning tunneling spectroscopy as a result of technical difficulties arising from the surface sensitivity. More accessible and

device-compatible tunneling spectroscopy can be achieved by fabricating planar tunnel junctions, where a metal probe is separated from the nanowire by a thin insulating barrier. Further, the use of a superconducting probe in a planar tunnel junction enables direct measurements of electron distribution functions and interactions, 11 along with enhanced spectroscopy of mesoscopic tunneling effects¹² and bound states. 13,14 Performing tunneling spectroscopy experiments where ballistic transport is maintained under the probe, high-quality tunnel barriers in conjunction with careful surface engineering of the nanowire is required to prevent the introduction of disorder. Aluminum is often used for tunnel junctions because the metal develops a well-controlled and self-limiting oxide layer. However, many semiconducting nanowires, including InSb, already have intrinsic surface oxides that are too thick for tunneling spectroscopy and typically contain a high defect density. Therefore, the native oxide layer needs to be removed—without introducing disorder into the wire—and replaced with a higher quality barrier material. In this letter, the systematic development of high-quality AlO_x tunnel barriers on InSb nanowires is described. Through the use of controlled etching, deposition, and oxidation techniques, nanowires having a low-roughness interface for the growth of pinhole-free AlOx tunnel barriers are realized. The quality of tunnel barrier fabrication is characterized using superconducting tunneling

^{a)}gill15@illinois.edu

b) nadya@illinois.edu

spectroscopy, which reveals a hard superconducting gap consistent with a uniform $\mathrm{AlO}_{\mathrm{x}}$ tunnel barrier. Additionally, in the device having uniform barriers, ballistic transport features such as Fabry-Perot resonances and quantized conductance steps are observed. Furthermore, the utility of tunnel junctions on InSb nanowires is demonstrated by performing nonequilibrium tunneling spectroscopy of an open quantum dot formed in an InSb nanowire, which reveals the presence of strong electronelectron interactions. The development of low-invasive tunnel junctions on InSb nanowires will allow for the characterization of the local density of states, which may find use in momentum resolved tunneling or characterizing the phase-dependence of Andreev bound states in nanowire Josephson junctions.

The devices presented in this paper use InSb nanowires that were grown by metal-organic vapor phase epitaxy¹⁵ and are deterministically transferred to chips having a SiO2 dielectric that was thermally grown on heavily p-doped Si. Si/SiO2 acts as a back gate for the nanowire. The SiO₂ substrate is prepatterned and then scrubbed of polymer debris using reactive ion etching prior to nanowire deposition. All contacts to the nanowires are defined by electron beam lithography (EBL). The devices reported in this paper were patterned in a three-terminal geometry consisting of two highly transparent normal metal contacts to InSb, separated by \sim 1 μ m, and a central superconducting tunnel probe. These devices enable the measurement of both two-terminal transport and tunneling spectroscopy to monitor the DOS in the electron cavity defined by the electrostatic profile of the probe. The transparent contacts are prepared using methods described elsewhere to realize ballistic InSb nanowire devices. 4,16,17 Following contact development, a probe is patterned using EBL, leaving a region of InSb nanowire coated in its native oxide. Following a brief reactive ion etch to remove any polymer remaining from lithography, the native oxide is removed using sulfur-based etching, which has been shown to leave a smooth InSb surface for further processing. 5,16 Prior to barrier deposition, the nanowire is briefly ion-milled to remove adsorbates following the wet etch step. To create the AlO_x barrier, 0.7 Å of Al was deposited at a rate of 0.1 Å/s followed by oxidation in high-purity O₂ at a pressure of 10 mTorr for 1 h. This deposition/oxidation step is then repeated two more times. Finally, a superconducting metal is deposited in situ on the barrier.

Figure 1(a) shows an SEM image of a completed device, while Fig. 1(b) shows the tunneling spectra from the superconducting probe

to InSb. Superconducting tunneling spectroscopy provides an excellent litmus test for the quality of the barrier because deviations from a BCS-like DOS can typically be linked to "leaks" and inhomogeneity in the barrier region. 18 As shown in Fig. 1(b), using our optimized recipe, a BCS-like DOS having a hard gap was observed when biasing the tunnel probe lead with one of the normal leads grounded. This indicates a low-leakage, low-disorder junction. It is also important that the deposition is minimally invasive to the nanowire, and ballistic transport can be maintained in the region under the probe. Figure 1(c) shows end-to-end conductance for the device shown in Fig. 1(a), where the signature "chess-board" pattern of Fabry-Perot interference as a function of gate voltage and source-drain voltage is evident, indicating quasiballistic conduction across the device.¹⁹ The Fabry-Perot patterns can be analyzed to compare the length of the ballistic region with the periodicity of gate voltage oscillations: the change in the Fermi wave vector over one period is given as $\delta k_F = \pi/L$, which is related to a change of carrier density by $2\delta k_F/\pi = C_{G,L}\Delta V_{G,FP}/e$, where $C_{G,L}$ is the gate capacitance per unit length of the cavity and $\Delta V_{\text{G,FP}}$ is the periodicity of the Fabry-Perot oscillations. Hence, the cavity length can be estimated as

$$L = \frac{2e}{\Delta V_{G,FP} C_{G,L}}. (1)$$

The gate capacitance in the region of the probe is negligible compared to the capacitance of the quantum point contacts to the gate, which is on the order of 5 aF. Using this approximation, the gate capacitance per unit length of the cavity is $C_{\rm G,L}\approx 10\,{\rm aF/\mu m}$. Given an average $\Delta V_{G,FP}$ of 55 mV, the cavity length is estimated to be L $\sim\!600\,{\rm nm}$, which is approximately the length from the center of one bare region of InSb to the next, as schematically shown in Fig. 1(a). Hence, the estimated cavity length agrees with the lithographically defined pattern, indicating quasiballistic transport along the entire nanowire, even under the superconducting tunnel probe.

The growth parameters that are required to realize a nearly ideal planar barrier, as sketched in Fig. 2(a), will now be discussed. From our experience, 18 an ideal barrier has a room temperature resistance above $100\,\mathrm{k}\Omega$, which allows the observation of a BCS-like density of states with a hard gap in the superconducting probe at low temperature. In general, depositing and oxidizing ultrathin films of Al on InSb do not guarantee a continuous barrier. Realistically, pinholes form

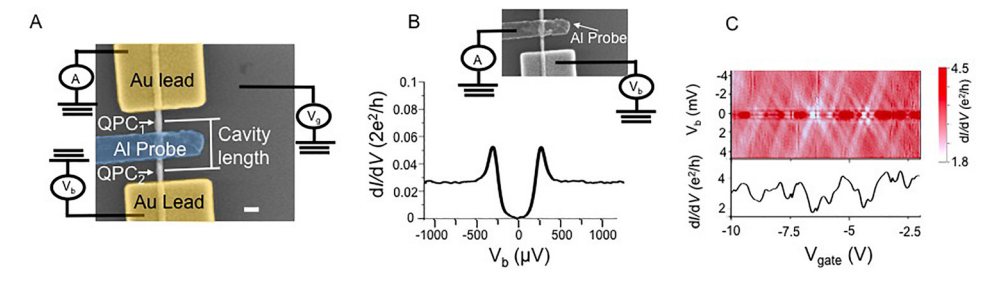


FIG. 1. (a) SEM image of a typical tunneling spectroscopy device, consisting of an Al probe and two Au leads. The bare constrictions form quantum point contacts (QPCs), which control the coupling of the cavity to the leads. In these experiments, the QPCs are tuned simultaneously using a global backgate. The scale bar in white is 200 nm. (b) Superconducing tunneling spectroscopy of the device in (a) at $V_g = 0$ V, showing a BCS-like density of states. The probe is grounded through a current preamp, while standard lock-in techniques are used to measure the conductance as a function of voltage bias. The measurement setup is shown schematically in the inset. (c) End-to-end conductance of the device in (a) as a function of gate voltage. The color map shows typical Fabry-Perot checkering as a function of gate and bias from interference in a ballistic electron cavity. The line cut from the color map is taken for $V_b = 0$ mV and shows that the oscillations are on the order of e^2/h .

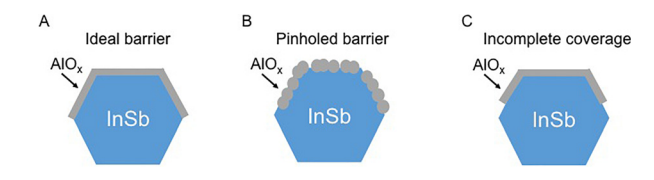


FIG. 2. (a) Cross-sectional schematic of an ideal, planar tunnel barrier on an InSb nanowire. (b) Cross-sectional schematic of a leaky, pinholed tunnel barrier. (c) Cross-sectional schematic of the shadowing effect from cold deposition of an AlO_x barrier.

from incomplete nucleation of AlO_x grains on the nanowire surface, as shown in Fig. 2(b). This motivated us to use liquid nitrogen to perform a cooled deposition of Al to promote the most continuous layer. However, as shown in Table I, barriers fabricated at low temperature and with a sticking layer before depositing the superconductor demonstrated resistances below what is required to observe a BCS-like DOS having a hard gap in tunneling measurements. Note that we define working superconducting tunnel junctions in Table I as those showing BCS-like peaks but having above gap conductance less than a factor of 10 greater than below gap conductance. In contrast, hard gap devices have above gap conductance greater than a factor of 10 than below gap conductance. The cold evaporation of ultrathin barriers likely leaves incomplete coverage on sides from shadowing, as shown in Fig. 2(c), which leaves a large area for the sticking layer to make a partial ohmic connection to the wire. To suppress any ohmic contact to the wire following barrier deposition, the superconductor was deposited without a sticking layer. 5 In doing so, the deposition of Al or NbTiN produces a high-resistance contact to InSb because of poor wetting of the metal on the semiconductor surface at room temperature. 5,16 After removing the sticking layer from our recipe, both cold and room temperature evaporation of the barrier could provide resistances that produced high-quality superconducting tunneling measurements at low temperatures. However, room temperature deposition of the barrier led to a higher yield of functioning tunnel junctions at low temperatures. We note that of the roughly 15 devices having optimal room temperature tunnel resistances and hard superconducting gaps at low temperature, ballistic transport features were also observed in endto-end measurements of the devices (last two rows in Table I). Given that ballistic transport is only observed in hard gap devices, we reveal the importance the uniformity of the tunnel barrier has on the transport characteristics in the device.

Figure 3 presents the properties of an optimized, nearly disorderfree device. For the data presented in Fig. 3, the tunnel barriers were deposited at room temperature and without a sticking layer. In Fig. 3(a), the magnitude of the tunnel conductance is independent of gate voltage, and the superconducting gap is seen over the entire scan with high clarity and no features forming below the gap, $\Delta_{\rm Al} = 220 \,\mu{\rm V}$. Figure 4(b) shows a tunneling measurement performed at zero gate voltage with the superconducting tunnel probe grounded, demonstrating a BCS-like DOS having an above-gap to subgap conductance ratio greater than 10, consistent with the deposition of a highly uniform tunnel barrier. The gate-independent magnitude of tunneling conductance and the absence of bound states observed below the superconducting gap attest to the high quality of the tunnel junction. Only above the gap can spectroscopic features from the nanowire be observed. Hence, these uniform, weakly coupling tunnel junctions allow for the characterization of the DOS in nanowires without significant contributions from probe-nanowire hybridization. Additionally, while this device was unable to fully pinch-off before dielectric breakdown, approximately quantized transport across the three-terminal geometry was observed, as shown in Fig. 4(c). The observation of roughly quantized conductance further confirms the uniformity of the barrier and low disorder impinged from fabricating the tunnel junction.

Finally, data are shown from an important application of superconducting tunnel probes: nonequilibrium tunneling spectroscopy. As shown in Fig. 4(a), this measurement involves applying a fixed voltage U across the device to drive the system out of equilibrium. The conductance across the tunnel junction is measured and is given by

$$\frac{\partial I}{\partial V_B}(V_B) = c \int_{-\infty}^{\infty} \frac{\partial n_{probe}(\mathbf{E})}{\partial E} n_{sample}(\mathbf{E} - \mathbf{e}V_B) \times \left[f_{sample}(\mathbf{E} - \mathbf{e}V_B) - f_{probe}(\mathbf{E}) \right] d\mathbf{E}, \tag{2}$$

where E is the energy relative to the Fermi energy, n_{probe} is the superconducting density of states in the probe, n_{sample} is the density of states in the 1D wire, and f_{probe} and f_{sample} are the Fermi distribution functions in the probe and the 1D wire, respectively. This expression 21 is a convolution of the electron energy distribution of the nanowire device with the voltage U with the DOS in the nanowire and the gradient of the DOS of the superconducting probe. Generally, the functional form of f_{sample} depends on how electrons are scattered as they travel down the nanowire. Figure 4(b) shows that as the nonequilibrium voltage is increased across the device, the gap shifts laterally while the peaks are smoothed out. Similar nonequilibrium behavior has been observed in carbon nanotubes and was associated with electron-electron scattering. Although the device measured in Fig. 4(b) has nonideal tunnel barriers,

TABLE I. List of superconducting materials used for probes, the barrier thickness, whether the barrier was deposited cold or a Ti sticking layer was used, the room temperature resistance range, number of devices fabricated, and the yield of superconducting tunnel junctions, hard gap junctions, and ballistic devices.

Probe material	Cold evaporation of the barrier	Ti sticking layer	Barrier thickness	T = 293 K probe resistances	Devices fabricated	Yield of superconducting tunnel junctions	Yield of hard gap junctions	Yield of ballistic devices
Al	Y	Y	2.1	$20-30\mathrm{k}\Omega$	20	0	0%	0%
NbTiN	Y	Y	2.1	$2040\mathrm{k}\Omega$	10	20%	0%	0%
Al	Y	Y	2.7	$6080\mathrm{k}\Omega$	20	30%	0%	0%
Al	Y	N	2.1	0.1 – $100+ M\Omega$	12	50%	50%	>50%
Al	N	N	1.9	$1100+M\Omega$	12	75%	75%	>75%

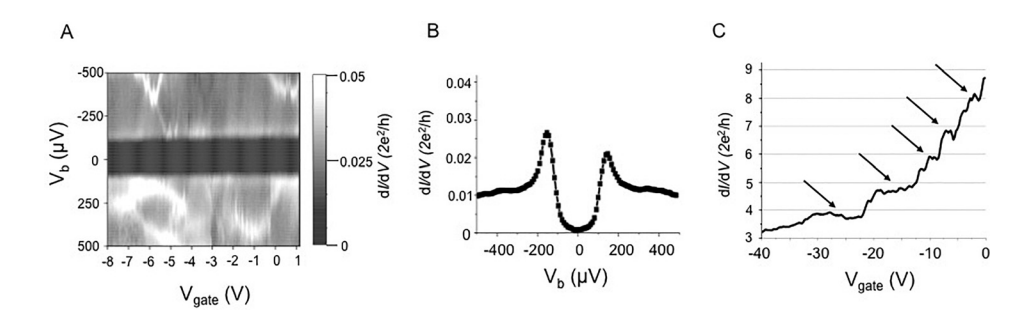


FIG. 3. (a) Gate dependence of the tunnel conductance as a function of bias. For the entire gate range, the magnitude of the tunnel conductance remains constant, and the superconducting gap is seen over the entire scan with high clarity and no features forming below the gap, $\Delta_{Al} = 220 \,\mu\text{V}$. (b) Plot of differential conductance as a function of bias for the tunnel junction. A hard gap is observed with an above gap to subgap conductance ratio greater than 10. The electron temperature is estimated to be 100–150 mK, resulting in slight thermal rounding of the gap. (c) Zero-bias end-to-end conductance as a function of gate showing plateaus, all of which are nearly quantized in units of 2 e²/h. Arrows point to plateau features in the conductance.

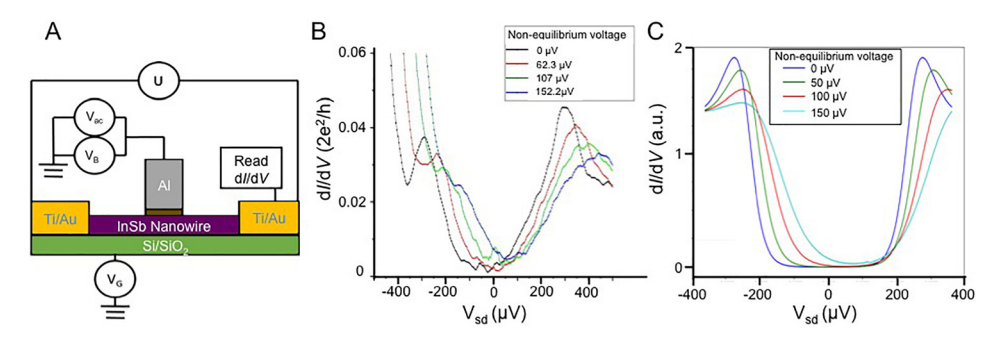


FIG. 4. (a) Schematic of nonequilibrium tunneling spectroscopy. A floating voltage, U, is applied across the ends while measuring the tunneling differential conductance of the superconducting probe as a function of bias. (b) Tunneling conductance as a function of nonequilibrium voltage. As the nonequilibrium voltage is increased across the device, the gap shifts laterally, while the peaks are smoothed out. (c) Simulation of the effect a nonequilibrium bias has on 1D wire having strong electron-electron scattering. Simulations show qualitatively similar behavior to the experimental device, implying strong electron-electron scattering in the device.

leading to a soft gap, it demonstrates the utilization of nonequilibrium superconducting tunneling spectroscopy on InSb nanowires and shows the nature of scattering caused by coupling the disorder of the nonideal barrier into the quantum wire. Indeed, as shown in Fig. 4(c), simulations of the impact that electron-electron scattering has on nonequilibrium superconducting tunneling spectroscopy possess strong qualitative resemblance to the experimental results. The simulations of the superconducting gap behavior with applied nonequilibrium voltage were performed following the procedure of previous work 12,20,21 and assumed that the nanowire device was thermalized to 250 mK and had a superconducting tunnel junction with $\Delta_{\rm AI} = 240~\mu{\rm V}$.

The methods presented here for fabricating high-quality tunnel junctions on high-mobility nanowires with strong spin-orbit coupling may have immediate applications for future studies of mesoscopic superconductivity. In a modified configuration of the same three-terminal geometry and by replacing the normal leads with superconducting leads, the phase-dependence of Andreev bound states in the InSb nanowire Josephson junction can be studied. ^{14,22} In addition, our work also lays the groundwork for developing thinner barriers that will enable proximity superconductivity in the wire and prevent deleterious metallization effects. ²³

In conclusion, high-quality tunnel junctions to ballistic cavities in InSb nanowire were developed. The performance of various barrier growth parameters and room temperature resistances that correspond to uniform, pinhole-free junctions was identified. Measurements confirmed that minimal disorder is added by the fabrication and that ballistic transport is maintained in the area under the tunnel junction. Superconducting tunneling spectroscopy demonstrated the high quality of the junction, and nonequilibrium tunneling spectroscopy was used to determine the extent of electron scattering. The use of high-quality tunnel junctions in quantum wires following the guidelines in this paper can be used to reveal salient features of helical modes and topological superconductivity in nanowire devices.

S.T.G., J.D., and N.M. were supported by the Office of Naval Research Grant Nos. N0014-16-1-2270 and NSF DMR-1710437. S.G, G.B., and E.P.A.M.B. were partly supported by the European Research Council and The Netherlands Organization for Scientific Research. S.T.G. acknowledges support from an NSF Graduate Research Fellowship. S.T.G., J.D., and N.M. acknowledge the use of the Materials Research Lab Central Facilities at the University of Illinois for all work.

REFERENCES

- ¹Ö. Gül, D. J. van Woerkon, I. van Weperen, D. Car, S. R. Plissard, E. P. A. M. Bakkers, and L. P. Kouwenhoven, Nanotechnology **26**, 215202 (2015).
- ²S. Nadj-Perge, V. S. Pribiag, J. W. van den Berg, K. Zuo, S. R. Plissard, E. P. Bakkers, S. M. Frolov, and L. P. Kouwenhoven, Phys. Rev. Lett. **108**(16), 166801 (2012).
- ³S. Gazibegovic, D. Car, H. Zhang, S. C. Balk, J. A. Logan, M. W. A. de Moor, M. C. Cassidy, R. Schmits, D. Xu, G. Wang, P. Krogstrup, R. L. M. Op het Veld, K. Zuo, Y. Vos, J. Shen, D. Bouman, B. Shojaei, D. Pennachio, J. S. Lee, P. J. van Veldhoven, S. Koelling, M. A. Verheijen, L. P. Kouwenhoven, C. J. Palmstrøm, and E. P. A. M. Bakkers, Nature 548, 434 (2017).
- ⁴S. T. Gill, J. Damasco, D. Car, E. P. A. M. Bakkers, and N. Mason, Appl. Phys. Lett. **109**, 233502 (2016).
- ⁵Ö. Gül, H. Zhang, F. K. de Vries, J. van Veen, K. Zuo, V. Mourik, S. Conesa-Boj, M. P. Nowak, D. J. van Woerkom, M. Quintero-Pérez et al., Nano Lett. 17, 2690 (2017).
- ⁶C. H. L. Quay, T. L. Hughes, J. A. Sulpizio, L. N. Pfeiffer, K. W. Baldwin, K. W. West, D. Goldhaber-Gordon, and R. de Picciotto, Nat. Phys. **6**, 336–339 (2010)
- ⁷Y. Oreg, G. Refael, and F. von Oppen, Phys. Rev. Lett. **105**, 177002 (2010).
- ⁸D. Rainis and D. Loss, Phys. Rev. B **90**, 235415 (2014).
- ⁹O. M. Auslaender, A. Yacoby, R. de Picciotto, K. W. Baldwin, L. N. Pfeiffer, and K. W. West, Science 295, 825 (2002).
- ¹⁰J. Reiner, A. K. Nayak, N. Avraham, A. Norris, B. Yan, I. C. Fulga, J.-H. Kang, T. Karzig, H. Shtrikman, and H. Beidenkopf, Phys. Rev. X 7, 021016 (2017).

- ¹¹T. Dirks, Y. F. Chen, N. O. Birge, and N. Mason, Appl. Phys. Lett. **95**, 192103 (2009).
- ¹²Y. F. Chen, T. Dirks, G. Al-Zoubi, N. O. Birge, and N. Mason, Phys. Rev. Lett. 102, 036804 (2009).
- ¹³T. Dirks, T. L. Hughes, S. Lal, B. Uchoa, Y.-F. Chen, C. Chialvo, P. M. Goldbart, and N. Mason, Nat. Phys. 7, 386 (2011).
- ¹⁴J.-D. Pillet, C. H. L. Quay, P. Morfin, C. Bena, A. L. Yeyati, and P. Joyez, Nat. Phys. 6, 965 (2010).
- ¹⁵S. R. Plissard, D. R. Slapak, M. A. Verheijen, M. Hocevar, G. G. W. Immin, I. van Weperen, S. Nadj-Perge, S. M. Frolov, L. P. Kouwenhoven, and E. P. A. M. Bakkers, Nano Lett. 12, 1794 (2012).
- ¹⁶S. T. Gill, J. Damasco, B. E. Janicek, M. S. Durkin, V. Humbert, S. Gazibegovic, D. Car, E. P. A. M. Bakkers, P. Y. Huang, and N. Mason, Nano Lett. 18, 6121 (2018).
- ¹⁷J. Kammhuber, M. C. Cassidy, H. Zhang, Ö. Gül, F. Pei, M. W. A. de Moor, B. Nijholt, K. Watanabe, T. Taniguchi, D. Car, S. R. Plissard, E. P. A. M. Bakkers, and L. P. Kouwenhoven, Nano Lett. 16, 3482 (2016).
- ¹⁸Y. Li and N. Mason, Appl. Phys. Lett. **102**, 023102 (2013).
- ¹⁹A. V. Kretinin, R. Popovitz-Biro, D. Mahalu, and H. Shtrikman, Nano Lett. 10, 3439 (2010).
- ²⁰N. Bronn and N. Mason, Phys. Rev. B **88**, 161409 (2013).
- ²¹H. Pothier, S. Gueron, N. O. Birge, D. Esteve, and M. H. Devoret, Phys. Rev. Lett. 79, 3490 (1997).
- ²²R. M. Lutchyn, J. D. Sau, and S. D. Sarma, Phys. Rev. Lett. **105**, 077001 (2010).
- ²³C. Reeg, D. Loss, and J. Klinovaja, *Phys. Rev. B* **97**, 165425 (2018).